Available online at www.sciencedirect.com
ScienceDirect
Journal of Solid State Chemistry 181 (2008) 802–811
JOURNAL OF SOLID STATE CHEMISTRY
www.elsevier.com/locate/jssc

# Structure and magnetic properties of potassium doped bismuth ferrite

Ja. Dhahri[a,b], M. Boudard[b,c,*], S. Zemni[a], H. Roussel[b], M. Oumezzine[a]

[a]*Laboratoire de Physico-Chimie des Matériaux, Département de Physique, Faculté des Sciences de Monastir, 5019 Monastir, Tunisia*
[b]*LMGP, MINATEC Bâtiment INPG, UMR 5628 CNRS/INPG, 3 Parvis Louis Néel, BP 257, 38016 Grenoble Cedex 1, France*
[c]*SIMAP/ENSEEG, UMR 5614 CNRS/INPG/UJF, BP 75, 38402 St. Martin d'Hères Cedex, France*

Received 25 July 2007; received in revised form 7 January 2008; accepted 13 January 2008
Available online 20 January 2008

**Abstract**

The influence of the potassium ($K^+$) doping on the structure of multiferroic $BiFeO_3$ and its relation with ferroelectric and magnetic properties was investigated for perovskites with composition $Bi_{1-x}K_xFeO_3$ in the range $0 \leqslant x \leqslant 0.07$. All the studied samples are described in $R3c$ space group (No. 161). Typical cell parameters ($BiFeO_3$) in hexagonal setting are $a_{hex} = 5.5769(2)$ Å and $c_{hex} = 13.8531(2)$ Å with $Z = 6$ formula units. The structure determination shows that as the $K^+$ content increases, the average cations displacements decrease reducing the polar character of doped samples with respect to pure $BiFeO_3$ and leading to a change from rhombohedral to a pseudo-cubic symmetry. A structural disorder is related to the substitution of $K^+$, which results in strong diffuse scattering (DS) located at the bottom of the Bragg peaks. Magnetic measurements reveal that all the compounds remain antiferromagnetic at room temperature (RT) with almost no change in the transition temperature (Néel temperature $T_N$).


*Keywords:* Perovskites; Multiferroics; Crystal structure; Symmetry; X-ray diffraction; Antiferromagnetic properties

## 1. Introduction

Multiferroic materials present a coexistence of electric, magnetic and/or ferroelastic orders. This coexistence leads to important physical properties and practical applications in magnetoelectronics and spintronics. Only few materials, especially perovskite oxides with *d*-electron metals, show such coexistence as, for example, $BiFeO_3$, $BiMnO_3$ and $YMnO_3$ (and other rare earth derived oxides) [1,2]. Coupling of the magnetic and ferroelectric orders leads to magnetoelectric effects. Recent theoretical and experimental studies show the influence of a modulated magnetic ordering on the value of electric polarization [3–6]. Related to this subject, different models of modulations have been recently re-considered in multiferroic $BiFeO_3$ revisiting the original interpretation of the magnetic ordering in terms of circular cycloid modulation (G-type antiferromagnetic order with a spatial modulation with a very large period of 620 Å [7]) [8]. Earlier investigations have been done on the $BiFeO_3$ perovskite [7,9–14]. X-ray single crystal and neutron powder diffraction studies showed that the structure of $BiFeO_3$ is rhombohedral with space group $R3c$ [10,12–17]. The development of spontaneous electric polarization along threefold axis ([111] pseudo-cubic direction) arises from relative displacement of the cations ($Bi^{3+}$, $Fe^{3+}$) against anions ($O^{2-}$) [10,15,16,18] with a relative high-phase transition temperature (Curie temperature, $T_C$, near 1100 K [10,11,19]). The G-type antiferromagnetic ordering takes place at lower temperatures ($T_N$ near 625 K) [9–11,17,20] with eventually a weak ferromagnetic component reported by some authors [10,21 and reference therein].

A lot of work has recently been done on multiferroic thin films (see for example, Refs. [22–25]). In particular, some discrepancies concerning the different values of the electric polarization in ceramics, single crystal and thin films of $BiFeO_3$ have been clarified and they appear to be related to the microstructure of the samples [10,19,21,26–29]. Doping $BiFeO_3$ with Mn also appears to modify the microstructure

*Corresponding author: SIMAP/ENSEEG, UMR 5614 CNRS/INPG/UJF, BP 75, 38402 St. Martin d'Hères Cedex, France.
Fax: +33 476826644.
*E-mail address:* mboudard@ltpcm.inpg.fr (M. Boudard).

0022-4596/$ - see front matter © 2008 Elsevier Inc. All rights reserved.
doi:10.1016/j.jssc.2008.01.024

of ceramics materials leading to a broadening of the diffraction peaks [7,30] and results in a transformation of the long-range spiral spin modulation toward a collinear antiferromagnetic structure [7]. As far as $K^+$ doping is concerned, thin films were investigated [31] but no pure $BiFeO_3$ phase was obtained. The films, obtained at different annealed temperatures, contained additional phases such as $Bi_2Fe_4O_9$ and no indication was given for the $K^+$ incorporation in these specimens. Due to the large size of $K^+$ ion with respect to $Bi^{3+}$ ($r_{K^+} = 1.64\,Å > r_{Bi^{3+}} = 1.17\,Å$ ionic radius [32]) one expected that doping will be difficult and will introduce a lot of disorder.

In this context and to understand the influence of the bismuth ($Bi^{3+}$) substitution by the potassium ($K^+$) on the physical properties of $BiFeO_3$, we have synthesized $K^+$ doped single crystals of $BiFeO_3$. The introduction of $K^+$ in the *A* site (*A* refers to Perovskite general formula $ABO_3$) can locally modify the *A* cation displacement and thus can perturb cooperative long-range ferroelectric order related to displacement of $Bi^{3+}$. It also results in a reduction of the average positive charge in the *A* site which needs to be compensated. This can be done by a deficiency of oxygen with a general non-stoichiometric formula $(Bi_{1-x}K_x)FeO_{3-\delta}$. Another compensation mechanism can be the increase of the average charge in the *B* site. This can results from modification of the valence of Fe ($Fe^{3+}$ changes to $Fe^{4+}$ with a general formula $(Bi_{1-x}K_x)FeO_3$) or by introduction in the *B* site of a small amount of $Bi^{5+}$ (the samples can be in this case considered as a solid solution of $BiFeO_3$ and $KBiO_3$ with a general formula $(Bi_{1-x}K_x)(Fe_{1-x}Bi_x)O_3$). According to these different mechanisms, the doping with $K^+$ could change the crystalline structure and the physical properties of $BiFeO_3$. In particular, the mixed valence state of Fe could play a major role in double exchange (DE) mechanism [33–35] which is responsible for the metallic character and ferromagnetic properties in oxides.

## 2. Experimental

### 2.1. Sample preparation and general characterization

Bismuth ferrite single crystals ($Bi_{1-x}K_xFeO_3$) were grown by the flux technique ($Bi_2O_3$ flux) in a platinum crucible with a 4/1 molar ratio ($4Bi_2O_3/1Fe_2O_3$). High-purity $Bi_2O_3$ (99.9%), $Fe_2O_3$ (99%) and $K_2CO_3$ (99.9%) powders were carefully weighted and thoroughly mixed in an agate mortar [10]. The mixture was heated at 1023 K for 12 h to achieve decarbonatization. After grinding, it was heated at 1133 K for 12 h and then cooled at a rate of 1 K/h to 1003 K, with an intermediate annealing time of 20 h at 1093 °K. The as-grown samples (presenting large single crystals) as well as an almost single-phase product obtained by dissolution of the flux with dilute nitric acid (hereafter cleaned sample (CS)) have been characterized by scanning electron microscopy (SEM) and powder and single crystal X-ray diffraction (XRD) techniques.

SEM observations on the as-grown material and the CS were made using a Philips XL30 and semi-quantitative analysis was performed at 15 kV accelerating voltage using energy dispersive X-ray analysis (EDX). No particular preparation was used (especially no flat surface was prepared by polishing) and eventually carbon coating was used to prevent charge phenomena. Precise chemical composition concerning relative cation contents was obtained from the CS by induced coupled plasma technique (ICP).

### 2.2. Magnetic measurements

Magnetization measurements ($M(T)$ and $M(H)$) were performed on powder samples obtained from the CS on magnetometers equipped with super conducting coils. High-temperature magnetometer with linear extraction at Louis Néel Laboratory (Grenoble, France) was used for studying the temperature dependence of the magnetization, $M(T)$, at 6 T magnetic field. $M(H)$ measurements at RT were measured with a Foner magnetometer with variable field $H$ between −4 and 4 T.

### 2.3. XRD experiments

Powder samples for XRD measurements were obtained from both as-grown material and CS. Si powder was added as an internal calibration for cell parameters determination and profile analysis. Bragg–Brentano reflection geometry was used on a Bruker D500 diffractometer (40 kV, 30 mA and $\lambda$ (Cu$K\alpha_1$) = 1.54062 Å). XRD patterns were obtained using 0.15° resolution slits in front of a scintillation counter and 0.04° step with 10 s counting time. They were analyzed by standard techniques (using CelRef, Eva and WinPLOTR [36–38]) to perform phase identification, cell parameters determination and line shape analysis.

Dark brown transparent single crystals (almost 100 μm in size) present in the as-grown and/or the CS were selected for the purpose of X-ray single crystal experiments. XRD data were collected at RT using an automatic Nonius Kappa diffractometer provided with a bi-dimensional (2-D) charge coupled device (CCD) detector. The Mo$K\alpha$ radiation ($\lambda = 0.71071$ Å) from sealed tube (50 kV and 35 mA) was selected with a graphite monochromator. Selected crystals present sharp diffraction peak corresponding to a pseudo-cubic perovskite. After determination of the crystal orientation matrix and shape, diffraction data were collected with the rotation technique by measuring $\omega$ and $\varphi$ scans frames of 2° oscillation angle with 200–480 s exposure times per frame. The sample to detector distance was set to 35 mm, and the maximum angle $\theta$ was 30°. Integrated diffracted intensities were extracted with the Eval14 software [39]. The Maxus suite [40] was used for data analysis. *E*-statistics suggested a possible non-centrosymmetric structure, and systematic extinction led to the selection of *R*3*c* as a possible space group (No. 161). Absorption correction was carried out using the

description of the crystal geometry and the Gaussian integration technique [41] (another absorption correction method using the semi-empirical method of the program Sortav [42] gives essentially the same results). Equivalent averaged reflections and structure refinements were carried out with the Shelxl program [43]. Measured reflections with intensity $I$ such that $I > 4\sigma(I)$ were used for refinements. Details are reported in Table 3.

The model of Kubel and Schmid [10] was used as input model. Bi (and K when present) coordinates were constrained to (0, 0, 0) and mixed sites Bi/K were used for $Bi_{1-x}K_xFeO_3$ samples with full occupancy constrained to ICP values. In the first stage of the refinement, all isotropic temperature factors were held constants ($u_{eq} = 0.01$ Å$^2$). In the second stage, anisotropic temperature factors were refined with fully occupied sites. Tables 3 and 4 present the results of the fit.

## 3. Experimental results and discussion

### 3.1. SEM observations and powder XRD

SEM observations on as-grown samples present generally two phases: a major phase ($Bi_2O_3$ type phase) and a minor phase corresponding to $Bi_{1-x}K_xFeO_3$ ($BiFeO_3$ type phase).

The SEM Z-contrast images show a uniform contrast within this phase. Several morphologies were observed indicating some non-homogeneity during the growing process although the general aspect corresponds to a primary crystallization of $Bi_{1-x}K_xFeO_3$ phase surrounded by an eutectic of $Bi_2O_3$ and $Bi_{1-x}K_xFeO_3$. The morphology of the crystals varies from a parallelepiped shape (with two main dimensions and a platelet shape) with juxtaposed regions corresponding to different domains for pure $BiFeO_3$, to a cubic shape for the crystals containing $K^+$.

EDX composition analysis shows that crystals with nominal composition $Bi_{1-x}K_xFeO_3$ ($0 \leqslant x \leqslant 0.6$) contains $K^+$ but with an amount much lower than the nominal one. Though EDX results are only semi-quantitative and cannot be taken for granted (see Section 2.1), this general tendency toward a much lower incorporation of $K^+$ was confirmed by precise chemical analysis obtained by ICP on the CS (reported in Table 1). The relative cation content for the undoped sample are in good agreement with the expected nominal values (i.e. Bi/Fe = 1). For the doped samples, the measured ratio is almost 15% of the nominal one (e.g. for nominal $x = 0.2$ we obtained only 0.03). We have thus

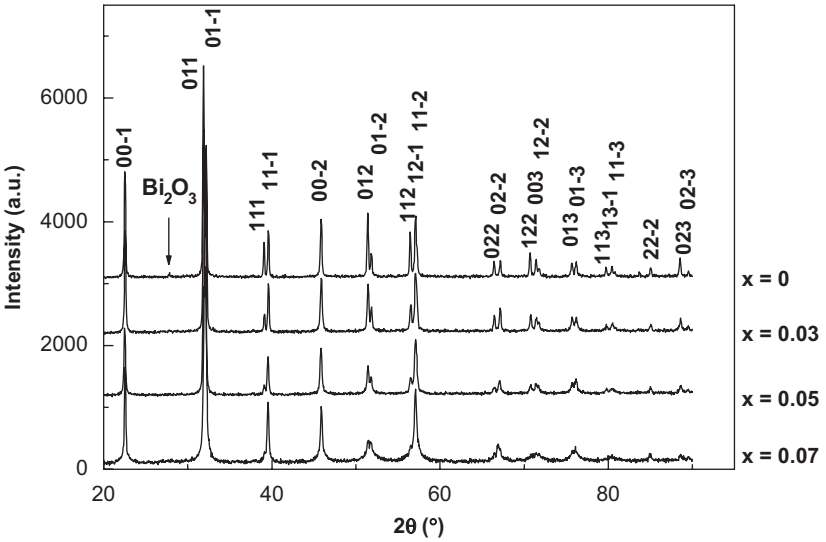


Fig. 1. Powder XRD patterns from CS of $Bi_{1-x}K_xFeO_3$ phase for $x = 0$, 0.03, 0.05 and 0.07. Indices of diffraction lines of $Bi1_{-x}K_xFeO_3$ phase correspond to a simple pseudo-cubic cell (cell parameter near 3.96 Å, see text). A small impurity diffraction line is marked as $Bi_2O_3$.

Table 1
Composition of the samples

| Nominal composition | ICP cation composition (at%) | | | Cationic formula |
|---|---|---|---|---|
| | Bi | Fe | K | |
| $BiFeO_3$ | 50.2±1.1 | 49.8±1.1 | – | $Bi_{1.01(2)}Fe_{1.00(2)}$ |
| $Bi_{0.8}K_{0.2}FeO_3$ | 48.5±1.1 | 50.1±1.1 | 1.4±0.3 | $Bi_{0.97(2)}K_{0.027(6)}Fe_{1.00(2)}$ |
| $Bi_{0.5}K_{0.5}FeO_3$ | 47.4±1.1 | 50.0±1.1 | 2.6±0.3 | $Bi_{0.95(2)}K_{0.052(7)}Fe_{1.00(2)}$ |
| $Bi_{0.4}K_{0.6}FeO_3$ | 46.5±1.1 | 49.9±1.1 | 3.6±0.3 | $Bi_{0.93(2)}K_{0.071(6)}Fe_{1.00(2)}$ |

Nominal, ICP and partial chemical formula derived from ICP analysis (uncertainties to the last significant digit are in parenthesis).

synthesized samples with nominal doping level of $K^+$ as high as 60% for $Bi_{1-x}K_xFeO_3$ ($0 \leqslant x \leqslant 0.6$), which allows to incorporate an increasing quantity of $K^+$ (Table 1). We suggest that the most representative chemical formula of our sample can be derived from the ICP results in Table 1 and should be $BiFeO_3$, $Bi_{0.97}K_{0.03}FeO_3$, $Bi_{0.95}K_{0.05}FeO_3$ and $Bi_{0.93}K_{0.07}FeO_3$ (respectively for nominal compositions: 0%, 20%, 50% and 60% of $K^+$) but no precise information was obtained for oxygen contribution (i.e. a more general chemical formula $Bi_{1-x}K_xFeO_{3-\delta}$ can be considered, see introduction). The retained chemical formula corresponds to partial transformation of $Fe^{3+}$ ion into $Fe^{4+}$ in the *B* site and a charge balanced chemical formula can be derived (e.g. $Bi_{0.93}K_{0.07}FeO_3$ leads to $(Bi^{3+}_{0.93}K^{+}_{0.07})(Fe^{3+}_{0.86}Fe^{4+}_{0.14})O^{2-}_3$). It should be noted that chemical formula with deficiency in oxygen can compensate the reduction of average positive charge in *A* site without changing the average charge in *B* site (see introduction). Though the presence of $Bi^{5+}$ in site *B* corresponding to $(Bi_{1-x}K_x)(Fe_{1-x}$ Bix$)O_3$ chemical formula (see introduction) appears improbable (Bi/Fe ratio should increase with $K^+$ content) its presence due to a more complicate scenario with non-stoichiometric formula cannot be excluded.

Powder XRD results agree with SEM results as far as identification of phases is concerned. Phase identification by XRD in the as-grown sample shows the presence of a $Bi_2O_3$ type phase (with either cubic or monoclinic cell depending on the samples) as the major phase and $BiFeO_3$ type phase (with rhombohedral cell) as minor phase. Occasionally the presence of a $Bi_2Fe_4O_9$ type phase (orthorhombic cell) was observed. CS powder XRD patterns (see Fig. 1) show the presence of an almost single phase ($BiFeO_3$ type) with a minor contribution of $Bi_2O_3$ (as indicated by an arrow in Fig. 1). When increasing the $K^+$ content the splitting of the XRD lines due to a rhombohedral cell is less important (Fig. 1) evolving toward a pseudo-cubic cell and the diffraction lines are characterized by an important diffuse scattering (DS) located at the bottom part of the Bragg peaks which is characteristic of an increasing disorder in the sample.

Precise values of the cell parameter *a* and the rhombohedral cell angle $\alpha$ (expressed in a rhombohedral setting close to a cubic cell) were obtained with Celref program from powder XRD pattern using Si as an internal calibration. Maximum difference between calculated and observed Bragg positions (including a zero shift correction) is 0.018° for $BiFeO_3$ and slightly larger for samples with $K^+$ content (0.068°) which results in less precise values (complete list of calculated and observed positions are available on request). We obtained the following results ($a_p$ corresponds to the primitive rhombohedral cell parameter ($a/2$) and $V_p$ is the corresponding primitive cell volume):

- $BiFeO_3$: $a_p = a/2 = 3.964(1)$ Å, $\alpha = 89.440(4)^\circ$, $V_p = 62.28(1)$ Å$^3$ (in good agreement with those found in the literature [10,11,15,44]);
- $Bi_{0.97}K_{0.03}FeO_3$: $a_p = a/2 = 3.962(2)$ Å, $\alpha = 89.480(2)^\circ$, $V_p = 62.22(4)$ Å$^3$;
- $Bi_{0.95}K_{0.05}FeO_3$: $a_p = a/2 = 3.961(2)$ Å, $\alpha = 89.560(1)^\circ$, $V_p = 62.17(3)$ Å$^3$;
- $Bi_{0.93}K_{0.07}FeO_3$: $a_p = a/2 = 3.956(2)$ Å, $\alpha = 89.88(2)^\circ$, $V_p = 61.95(3)$ Å$^3$.

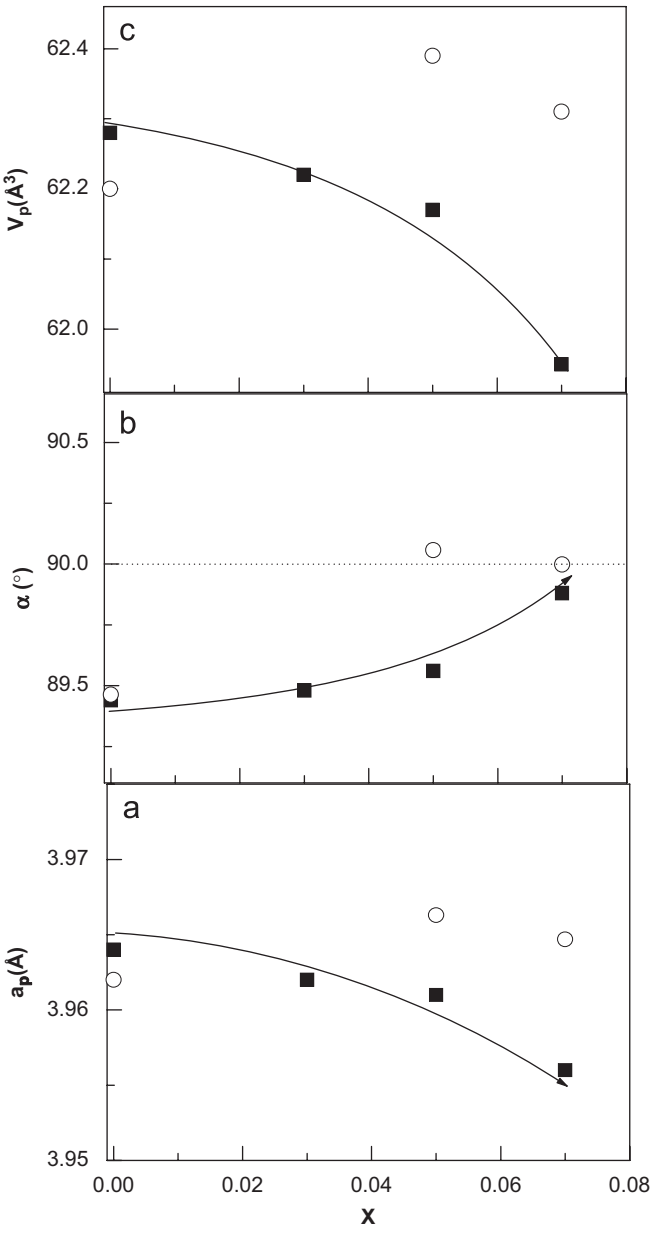


Fig. 2. Comparison of the evolution of the rhombohedral cell (expressed in rhombohedral setting close to primitive basic perovskite cubic cell) for $Bi_{1-x}K_xFeO_3$ as a function of *x* (■: powder, ○: single crystal). (a) $a_p$ primitive rhombohedral (see text) cell parameter in Å. (b) $\alpha$ cell angle in degrees. (c) $V_p$ primitive rhombohedral cell volume. Dashed line in (b) represents the 90° angle corresponding to cubic symmetry. Solid lines in both figures are guides for the eyes. Difference between powder and single crystal data may be due to pseudo-symmetry effects that can arise from coherent twinning leading to an enhancement of the pseudo-cubic symmetry.

As the $K^+$ content increases, there is an evolution toward a pseudo-cubic symmetry (Fig. 2): the $a_p$ parameter diminishes and the angle increases resulting in a slight reduction of the cell volume. Difference between powder and single crystal data in Fig. 2 may be due to pseudo-symmetry effects that can arise from coherent twinning leading to an enhance of the pseudo-cubic symmetry for single crystals.

Fig. 3 and Table 2 show the results of a line shape analysis on powder XRD corresponding to composition used in single crystals studies ($BiFeO_3$, $Bi_{0.95}K_{0.05}FeO_3$ and $Bi_{0.93}K_{0.07}FeO_3$). XRD lines corresponding to $BiFeO_3$ can be fitted considering a main component represented by a pseudovoigt function (PV) with a mixture parameter $\eta$ ($\eta = 0$ corresponds to a Gaussian function and $\eta = 1$ to a Lorentzian function) ranging from 0.3 to 0.45 and a full-width half-maximum (FWHM) ranging from 0.18° to 0.2° (for the XRD line near 46° in $2\theta$ a small component with $\eta = 0.5$ take into account a disorder, though it is relatively small representing 20% of the overall intensity). These values are similar to the values obtained from the Si powder mixed to the CS which are characterized by a main contribution represented by a PV with $\eta = 0.2$ and FWHM ranging from 0.15° to 0.18°. Thus, $BiFeO_3$ appears as a well-crystallized sample with

Table 2
Results of the analysis of the peaks profiles for $Bi_{1-x}K_xFeO_3$ samples with $x = 0$, 0.05 and 0.07

| $x$ | $2\theta$ (deg) | $I$ (a.u.) | FWHM (deg) | $\eta$ |
|---|---|---|---|---|
| 0 | 22.49 | 376 | 0.187 | 0.40 |
| | 45.82 | 214 | 0.198 | 0.30 |
| | 45.82 | 61 | 0.651 | 0.50 |
| | 51.37 | 219 | 0.191 | 0.40 |
| | 51.80 | 101 | 0.205 | 0.45 |
| 0.05 | 22.50 | 451 | 0.200 | 0.20 |
| | 22.50 | 384 | 0.558 | 0.60 |
| | 45.84 | 265 | 0.220 | 0.30 |
| | 45.84 | 388 | 0.649 | 0.60 |
| | 51.41 | 178 | 0.259 | 0.20 |
| | 51.41 | 298 | 0.910 | 0.95 |
| | 51.79 | 167 | 0.252 | 0.50 |
| 0.07 | 22.55 | 302 | 0.185 | 0.20 |
| | 22.55 | 294 | 0.998 | 0.95 |
| | 45.88 | 171 | 0.216 | 0.20 |
| | 45.88 | 343 | 0.979 | 0.98 |
| | 51.41 | 101 | 0.310 | 0.35 |
| | 51.81 | 114 | 0.364 | 0.50 |

For each $x$ ($K^+$ proportion) the main characteristic of the different component used in the fitting procedure are summarized from left to right: position in $2\theta$ (in degrees), intensity $I$ (in arbitrary units), FWHM (in $2\theta$) in degrees and $\eta$ mixing parameter of the pseudo-Voigt function.

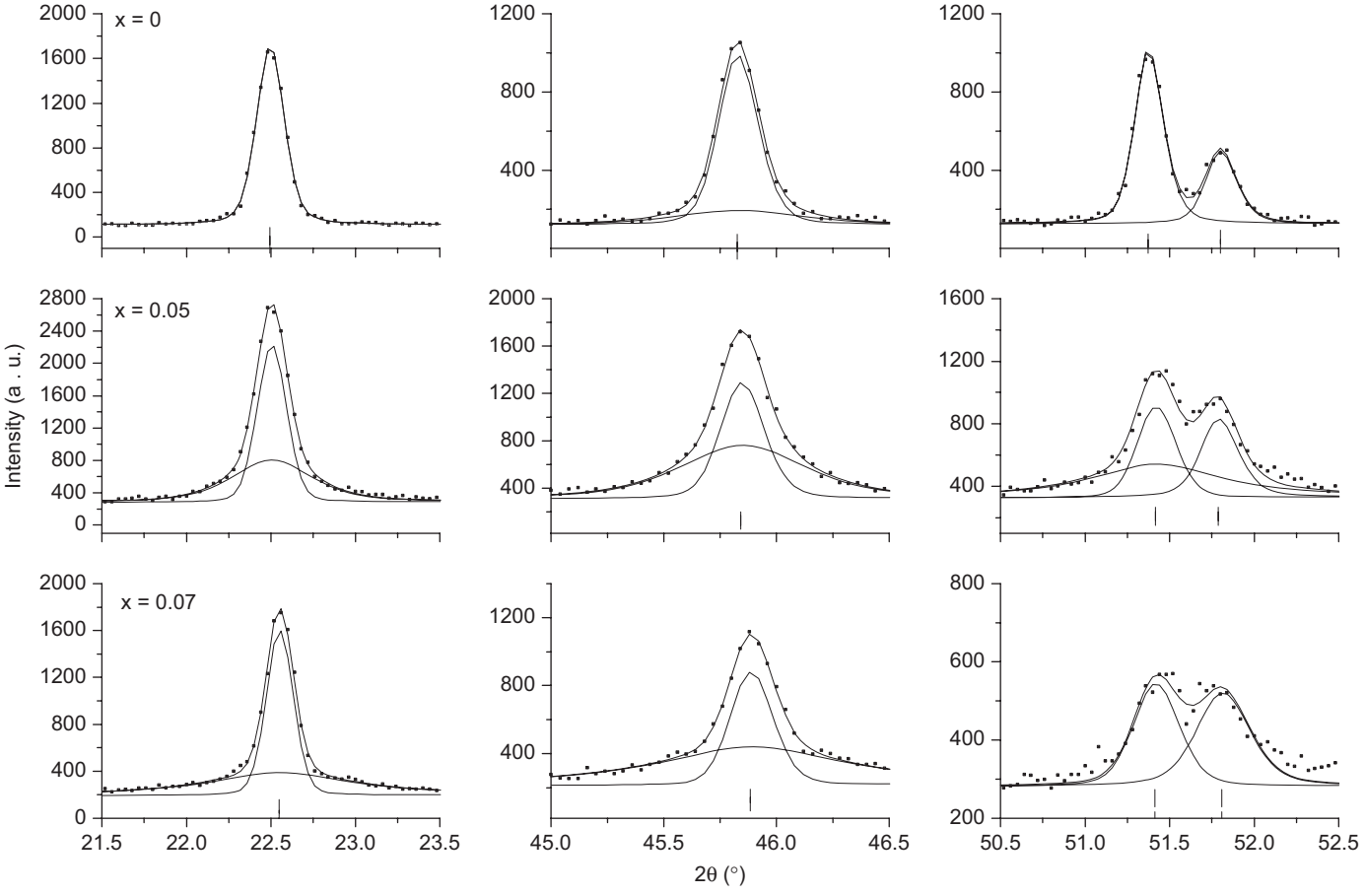


Fig. 3. XRD profile analysis of $Bi_{1-x}K_xFeO_3$ phase for $x = 0$, 0.05 and 0.07. Solid lines and vertical bars correspond to the results of the fitting procedure (see Table 2). The FWHM of the diffraction lines as well as the DS located at the bottom of the Bragg peaks are increasing with $K^+$ content.

small amount of defects (no major broadening due to size effect and/or strain). XRD lines corresponding to $Bi_{1-x}K_xFeO_3$ generally present an additional contribution, corresponding to DS located at the bottom of the Bragg contribution, with larges $\eta$ (0.6–0.98) and FWHM (0.55–0.99) parameters representing more than 50% of the overall intensities and corresponding to an increasing disorder related to the addition of $K^+$ (DS contribution at the bottom right in Fig. 3 is included in the two PVs which present relatively large FWHM and $\eta$ parameters. In this case, the identification of the individual component corresponding to the DS (not done) is arbitrary due to the mixing of the two components of the different XRD lines and due to the weakness of the signal). These features will be important when discussing single crystal XRD results.

Preliminary work on the DS with XRD on single crystal sample containing $K^+$ which have the more intense diffuse scattering ($x = 0.07$) was carried out by omega scan with 0.05° step over a large region (8° in $\theta$) and very long counting time (6000 s/°). The CCD camera was set at 165 mm. Three peaks were investigated (2, 0, 0) (2, 1, 0) and (3, 2, 0). Indices are in primitive rhombohedral (close to cubic) setting. Large region of DS appears at the bottom of the Bragg peaks and in particular is quite strong for (3, 2, 0) (weak) reflection. This DS is uniform with no clear anisotropy.

### 3.2. Single crystal XRD: description of the structures and discussion related to ferroelectric properties

According to Megaw and Darlington [45] two points are important when describing the structure of the single crystal $Bi_{1-x}K_xFeO_3$:

- displacement of bismuth and iron ions along the $c_{hex}$ axis (hexagonal) leading to polar ferroelectric character ($s$ and $t$ parameters are defined below),
- distortion ($d$ parameter is defined below) and rotation ($e$ parameter is defined below) of the octahedrons.

The parameters $s$, $t$, $d$ and $e$ are related to the atomic coordinates of a rhombohedral perovskite $ABO_3$ described in the hexagonal setting for $R3c$ space group as follows (these positions are equivalent to those reported in Table 4 after applying a global shift of (0, 0, 0.25):

$$A(\mathrm{Bi, K})(0, 0, s + 0.25),$$

$$B(\mathrm{Fe})(0, 0, t),$$

$$\mathrm{O}(1/6 - 2(e + d), 1/3 - 4d, 1/12),$$

where $s$ and $t$ are respectively, the fractional shift of the $A$ and $B$ cations along the pseudo-cubic [111] ($c_{hex}$) axis, $d$ is related to the difference of area of opposite triangular faces of the octahedron along the pseudo-cubic [111] axis and the parameter $e$ is related to the angle of tilt, $w$, around pseudo-cubic [111] axis by the following relation:

$$\tan(w) = 4e\sqrt{3}.$$

Though the results obtained in the present work for $BiFeO_3$ are almost identical to those obtained by Kubel and Schmid [10], clear differences appear when increasing the $K^+$ content (see Table 4 and Fig. 4). $BiFeO_3$ (pure and $K^+$ doped) are characterized by $R3c$ space group with cations displacement along the $c_{hex}$ axis and antiphase $\boldsymbol{a}^-\boldsymbol{a}^-\boldsymbol{a}^-$ oxygen octahedral tilts with a doubling of the primitive perovskite cell characterized by weak superstructure reflections (almost vanishing for $Bi_{0.93}K_{0.07}FeO_3$). The $Bi^{3+}$ and $Fe^{3+}$ cations are displaced with respect to the center of mass of their coordination polyhedra formed by $O^{2-}$ anions resulting in the polar character of this ferroelectric phase [15,46]. When increasing the $K^+$ content the polar ferroelectric character of the structure is reduced (see Table 4 and Fig. 4 [47]) essentially due to the larger reduction of $\Delta_{Bi-O}$ which is accompanied by a

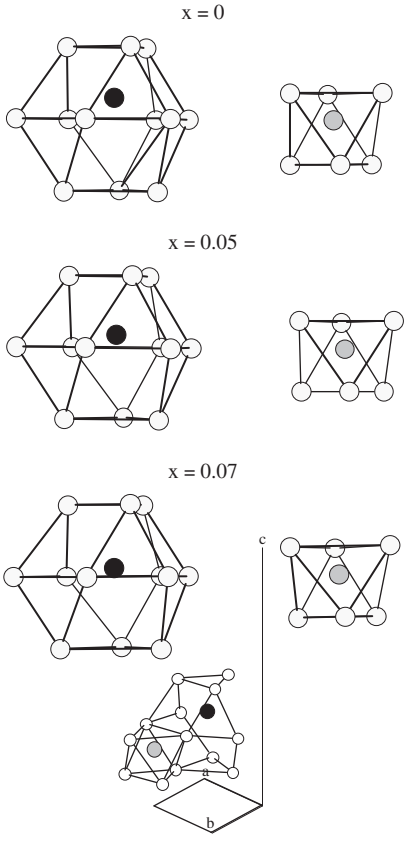


Fig. 4. Coordination polyhedra of $Bi_{1-x}K_xFeO_3$ samples with $x = 0$, 0.05 and 0.07. Left panel: cuboctahedron (around Bi/K). Right panel: octahedron (around Fe). Anions and cations are represented as balls: white (O), gray (Fe) and Bi/K (black). Note the displacement along the $c_{hex}$ axis (vertical direction of the figure) of the cations (with respect to the center of the coordination polyhedra), which diminishes with $K^+$ content. This situation results from the shift of oxygen anions $O^{2-}$ and $Fe^{3+}$ cations (the Bi/K cations are fixed at the origin) from the ideal cubic perovskite position combined with the deformation of the cell. Relative arrangement of the polyhera with respect to the hexagonal cell is represented in the bottom part. Carine software was used [47].

smaller variation of $\Delta_{Fe-O}$ (which results in almost vanishing superstructure reflections for high $K^+$ content single crystal). The ferroelectricity is also related to the difference between the Bi–Fe distances along the threefold axis which are respectively (3.065, 3.307, 3.575, 3.861 in Å), (3.27, 3.38, 3.49, 3.59 in Å) and (3.41, 3.42, 3.44, 3.45 in Å) for $BiFeO_3$, $Bi_{0.95}K_{0.05}FeO_3$ and $Bi_{0.93}K_{0.07}FeO_3$. These distances are nearly equal for $Bi_{0.93}K_{0.07}FeO_3$ and are compatible with a structure close to pseudo-cubic symmetry with a decrease of ferroelectricity.

When increasing the $K^+$ content the tilt of the oxygen octahedron is almost constant (it changes from 12.6° for $BiFeO_3$ to 14° for $Bi_{0.93}K_{0.07}FeO_3$) whereas its distortion increases ($d$ parameter changes from magnitude of 0.005 for $BiFeO_3$ to 0.01 for $Bi_{0.93}K_{0.07}FeO_3$). This distortion corresponds to a difference in the two triangular faces along the $c$ axis with small and large O–O distances. The small (large) O–O distances are 2.71(3.01) Å, 2.69(3.07) Å and 2.54(3.21) Å, respectively, for $BiFeO_3$, $Bi_{0.95}K_{0.05}FeO_3$ and $Bi_{0.93}K_{0.07}FeO_3$. The other O–O distances in the octahedron of the $Bi_{1-x}K_xFeO_3$ compounds are nearly equal to 2.80 and 2.89 Å. The O in the large and small triangular faces correspond respectively to short and long Fe–O distance which are respectively (1.941, 2.127 in Å), (1.99, 2.09 in Å) and (2.02, 2.06 in Å) for $BiFeO_3$, $Bi_{0.95}K_{0.05}FeO_3$ and $Bi_{0.93}K_{0.07}FeO_3$. The increase of the difference in small and large triangular faces is accompanied by the reduction of the difference between short and long Fe–O bonds.

The present structural parameters have to be considered as representative of an average structure. Crystals containing $K^+$ are not well ordered crystals and contain a lot of DS. It results a worst agreement factor (w$R$) especially when weak reflections are taken into account (which will be more affected by the DS). Powder XRD measurements clearly show that the large amount of DS is increasing with $K^+$ content. This DS is partially taken into account by large Debye Waller (DW) factor when working with our single crystal data. Indeed these values are abnormally high for crystal containing $K^+$ and reflect a large disorder introduced by the $K^+$ ion (see Table 4).

This disorder is difficult to precise with the present fitting strategy and three additional studies (in progress) were used: (1) search of minimum of residual factors as a function of oxygen positions, (2) analysis of residual electron density maps and (3) twins or statistical disorder are considered as the final stage of refinement.

$BiFeO_3$ shows a clear unique minimum of residual factor as a function of oxygen position and a residual electron density, which can be attributed to a minor contribution due to additional domains [10].

Multiple and not well-defined minima in the residual factor as a function of oxygen position were identified for $K^+$ doped samples. They could correspond to domains or statistical disorder (we found difficult to distinguish between twin and statistical disorder). Table 4 reports a unique oxygen position close to the one in $BiFeO_3$ (fixed DW factors components were used to avoid unphysical high values). Preliminary refinement including complex twin (or multiple positions corresponding to statistical disorder) leads to almost the same results as those presented in Tables 3 and 4.

Table 3
Experimental conditions and refinement parameters of $BiFeO_3$, $Bi_{0.95}K_{0.05}FeO_3$ and $Bi_{0.93}K_{0.07}FeO_3$

| | $x=0$ | $x=0.05$ | $x=0.07$ |
|---|---|---|---|
| Crystal size ($mm^3$) | 0.000315 | 0.0000155 | 0.000021 |
| $\mu$ ($mm^{-1}$), $T_{min}$, $T_{max}$ | 76.20, 0.018, 0.11 | 77.63, 0.19, 0.299 | 77.73 ,0.16 ,0.57 |
| $(\sin\theta/\lambda)_{max}$ ($Å^{-1}$) | 0.7024 | 0.592 | 0.701 |
| Range of $h,k,l$ | $-7\leqslant h\leqslant 7$ | $-6\leqslant h\leqslant 6$ | $-7\leqslant h\leqslant 7$ |
| | $-7\leqslant k\leqslant 7$ | $-6\leqslant k\leqslant 7$ | $-6\leqslant k\leqslant 7$ |
| | $-19\leqslant l\leqslant 19$ | $-16\leqslant l\leqslant 15$ | $-19\leqslant l\leqslant 18$ |
| $N_{Total}$ (unique, unique$>4\sigma$) | 7182(243, 213) | 1033(144, 122) | 3920(235, 166) |
| Number of parameters | 13 | 13 | 15 |
| $R_{int}$ (%) | 11 | 5 | 11 |
| $R$ (w$R$) (%) | 0.036(0.11) | 4.5(8.9) | 5(12) |
| Goodness-of-fit, $S$ | 0.894 | 1.17 | 1.2 |
| $\Delta\rho_{max}$, $\Delta\rho_{min}$ ($e\,Å^{-3}$) | 5.7–1.8 | 1.78–1.53 | 3.13–2.15 |
| $Z$ | 6 | 6 | 6 |
| $a_{hex}$ (Å) | 5.5769(2) | 5.6120(2) | 5.6069(2) |
| $c_{hex}$ (Å) | 13.8531(2) | 13.7260(2) | 13.7346(2) |
| $V_{hex}$ ($Å^3$) | 373.13(3) | 374.38(3) | 373.90(3) |
| $a_p$ (Å) | 3.962 | 3.966 | 3.965 |
| $\alpha$ (°) | 89.46 | 90.05 | 89.99 |
| $V_p$ ($Å^3$) | 62.20 | 62.39 | 62.31 |

$\mu$ corresponds to the linear absorption coefficient, $T_{min}$ and $T_{max}$ are the minimum and maximum transmission. $N_{Total}$ is the total number of reflections collected. In bracket unique and unique data with $F^2>4\sigma$ ($F^2$) used in the refinement ($F$-structure factor). The weighted $R$-factor (w$R$) and goodness-of-fit ($S$) are based on $F^2$, conventional $R$-factors ($R$) are based on $F$. The threshold expression of $F^2>4\sigma$ ($F^2$) were used for $R$, w$R$ and $S$. Cell parameters and volume in hexagonal ($a_{hex}$, $c_{hex}$, $V_{hex}$) and primitive rhombohedral ($a_p$, $\alpha$, $V_p$) settings.

Table 4
Different structural parameters obtained from the fit with e.s.d.'s in parentheses for $Bi_{1-x}K_xFeO_3$ samples for $x = 0$, 0.05 and 0.07

| | | | $x = 0$ | $x = 0.05$ | $x = 0.07$ |
|---|---|---|---|---|---|
| Positional parameters | Bi/K | $x = y = z$ | 0 | 0 | 0 |
| | Fe | $x = y$ | 0 | 0 | 0 |
| | | $z$ | 0.2212(3) | 0.238(3) | 0.248(3) |
| | O | $x$ | 0.445(2) | 0.442(6) | 0.45(1) |
| | | $y$ | 0.018(2) | 0.02(1) | 0.04(1) |
| | | $z$ | 0.9503(9) | 0.970(3) | 0.980(3) |
| s.o.f. | Bi/K | | 0.333 | 0.316/0.016 | 0.307/0.023 |
| | Fe | | 0.333 | 0.333 | 0.333 |
| | O | | 1 | 1 | 1 |
| Anisotropic temperature parameters (Å$^2$) | Bi/K | $U_{11} = U_{22} = 2U_{12}$ | 0.0082(4) | 0.026(1) | 0.0223(8) |
| | | $U_{33}$ | 0.0089(5) | 0.027(1) | 0.023(1) |
| | | $U_{13} = U_{23}$ | 0 | 0 | 0 |
| | | $U_{eq}$ | 0.0085(4) | 0.026(1) | 0.0227(8) |
| | Fe | $U_{11} = U_{22} = 2U_{12}$ | 0.006(1) | 0.060(4) | 0.056(3) |
| | | $U_{33}$ | 0.008(1) | 0.06(2) | 0.047(4) |
| | | $U_{13} = U_{23}$ | 0 | 0 | 0 |
| | | $U_{eq}$ | 0.0072(7) | 0.060(6) | 0.053(2) |
| | O | $U_{11}$ | 0.010(4) | 0.03(2) | 0.04(2) |
| | | $U_{22}$ | 0.002(4) | 0.06(2) | 0.04(2) |
| | | $U_{33}$ | 0.008(3) | 0.10(3) | 0.08(2) |
| | | $U_{12}$ | 0.002(4) | 0 | 0 |
| | | $U_{13}$ | 0 | 0 | 0.00(2) |
| | | $U_{23}$ | −0.001(3) | 0 | 0.02(2) |
| | | $U_{eq}$ | 0.008(2) | 0.07(1) | 0.06(1) |
| Bond distances (Å) | $\delta_{Bi/K-O}$ | | 2.25(9), 2.526(3), 3.223(2), 3.46(1) | 2.44(4), 2.46(3), 3.23(4), 3.22(3) | 2.44(4), 2.49(4), 3.16(4), 3.20(4) |
| | $\delta_{Bi-Fe}$ | | 3.065(4), 3.307(1), 3.575(2), 3.862(4) | 3.27(4), 3.38(1), 3.49(2), 3.59(4) | 3.41(5), 3.42(2), 3.44(2), 3.45(5) |
| | $\delta_{Fe-O}$ | | 1.941(6), 2.127(8) | 1.99(5), 2.09(5) | 2.02(6), 2.06(6) |
| | $\delta_{O-O}$ | | 2.71(2), 2.822(2), 2.861(4), 3.01(2) | 2.69(8), 2.810(6), 2.86(2), 3.07(8) | 2.54(7), 2.803(8), 2.89(2), 3.21(7) |
| Selected angles (deg) | $\theta_{Fe-O-Fe}$ | | 153.8(6) | 153(2) | 152(2) |
| | $\theta_{O-Fe-O}$ | | 87.7(2), 89.3(2), 101.7(5), 163.7(7) | 87.1(6), 89.2(7), 101(2), 165(3) | 78(2), 87(1) 103(2), 162(3) |
| Shift of atoms (Å) | $\Delta_{Fe-O}$ | | 0.29 | 0.25 | 0.25 |
| | $\Delta_{Bi-O}$ | | 0.69 | 0.41 | 0.27 |
| Tilt of octahedron (deg) | | | 12.6(6) | 13(2) | 14(3) |

s.o.f.: site occupancy factor; $U_{eq}$: equivalent isotropic temperature factor. The shift of atoms is along $c_{hex}$ direction.

As a conclusion of this section, we can say that the evolution of cell parameters and single crystal structure determination as a function of $K^+$ content suggest that the rhombohedral structure evolves toward a pseudo-cubic structure as a consequence of disorder induced by $K^+$. The microscopic nature of this disorder remains however difficult to identify (twinning, statistical disorder, …). As far as the average structure is considered there is a reduction of the ferroelectric character of this phase with the increasing of $K^+$ content related to the reduction of the cation shifts.

### 3.3. Magnetic properties

Fig. 5 shows the evolution of magnetization as a function of magnetic field $M(H)$ for samples of $Bi_{1-x}K_xFeO_3$ phase with $x = 0$, 0.03 and 0.07. The results obtained with Foner magnetometer at RT and with magnetic field varying from −4 to 4 T show that all measured compounds $Bi_{1-x}K_xFeO_3$ exhibit an antiferromagnetic behavior that appears as an almost linear contribution with a slope decreasing with the increase in $K^+$ contents. This figure displays also a very weak ferromagnetic contribution especially for $x = 0$ sample (see a little hysteresis loops for these curves in the inset). It is difficult to conclude if it is due to $BiFeO_3$ phase or to some impurity.

Fig. 6 shows the results of the evolution of the magnetization with temperature, $M(T)$, measured with an applied magnetic field of 6 T for $Bi_{1-x}K_xFeO_3$ with $x = 0$, 0.03 and 0.05. For all the samples, one can observe a transition from a paramagnetic phase at high temperature to an antiferromagnetic phase at low temperature corresponding to an abrupt decrease of the magnetization as temperature is lowered. Half the mass, with respect to $x = 0$ and 0.03, was used for $x = 0.05$ and measurement of sample $x = 0.07$ was impossible due to the very small

amount of sample that was available for this experiment. It is difficult to determine exactly the value of $T_N$ from these curves and we suggest that it is situated in an interval as indicated in Table 5. For $BiFeO_3$ this result is agreeing in particular with the work of Bucci et al. [44] who shows that the cell parameter (XRD study) have a discontinuity with temperature located between 598 and 617 K. Note that $M(T)$ curve for $x = 0$ also shows a discontinuity in the slope that is marked with an arrow in Fig. 6. This feature is disappearing with $K^+$ level doping at the same time that the amplitude of the magnetization decreases (see also Fig. 5) and could be related to an increase in the antiferromagnetic character. The structure evolution with $K^+$ content suggests a decrease of bond angles Fe–O–Fe from 153.8° to 152° (see Table 4) that enhances the superexchange Fe–O–Fe interactions and consequently reinforces the antiferromagnetic behavior. As there is no ferromagnetic enhancement we think that $K^+$ doping do not affects the valence of Fe ions and a different charge compensation mechanism could be present (see Section 3.1). A transformation of the magnetic order similar to the one induced by Mn doping in $BiFeO_3$ [7] could be considered. Doping $BiFeO_3$ with Mn appears to modify the microstructure of ceramics materials leading to a broadening of the diffraction peaks and results in a transformation of the long-range spiral spin modulation toward a collinear antiferromagnetic structure. Similarly, $K^+$ doping induced a large amount of disorder that could destroy the very long range spiral modulation transforming toward a more strong antiferromagnetic structure.

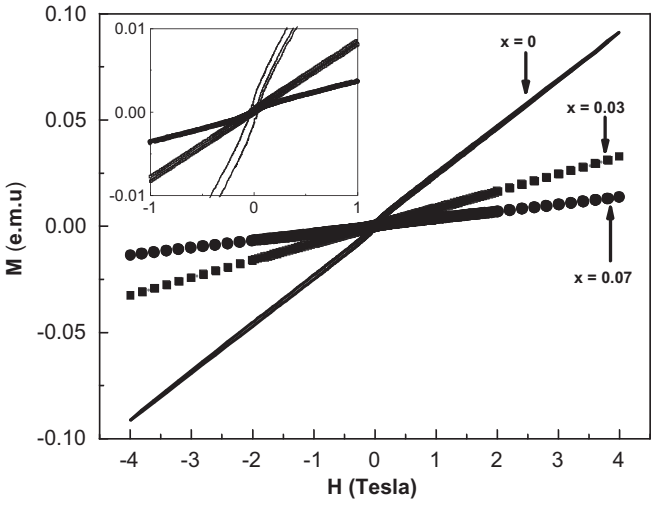


Fig. 5. $M(H)$ magnetization vs. field curves measured at RT for samples of $Bi_{1-x}K_xFeO_3$ phase for $x = 0$, 0.03 and 0.07. The inset represent an enlargement of the central part of the curve $M(H)$ showing a small hysteresis especially for $x = 0$ sample.

## 4. Conclusion

We have studied the effects of $K^+$ substitution within the sites of Bi, with respect to the structural and magnetic properties of $Bi_{1-x}K_xFeO_3$ single crystal perovskites

Table 5
Values of $T_N$ and maximum values of the magnetization ($M_{max}$) for $Bi_{1-x}K_xFeO_3$ and $x = 0$, 0.03 and 0.05

| $x$ | $T_N$ (K) | $M_{max}$ ($\mu_B$/f.u.) | $M_{max}$ (e.m.u./g) |
|---|---|---|---|
| 0 | 590–654 | 0.0333 | 0.5950 |
| 0.03 | 580–653 | 0.0296 | 0.5232 |
| 0.05 | 560–648 | 0.0223 | 0.4100 |

Minimum values of $T_N$ correspond to $M_{max}$. Maximum values of $T_N$ correspond to the sudden raise of $M$ when lowering the temperature.

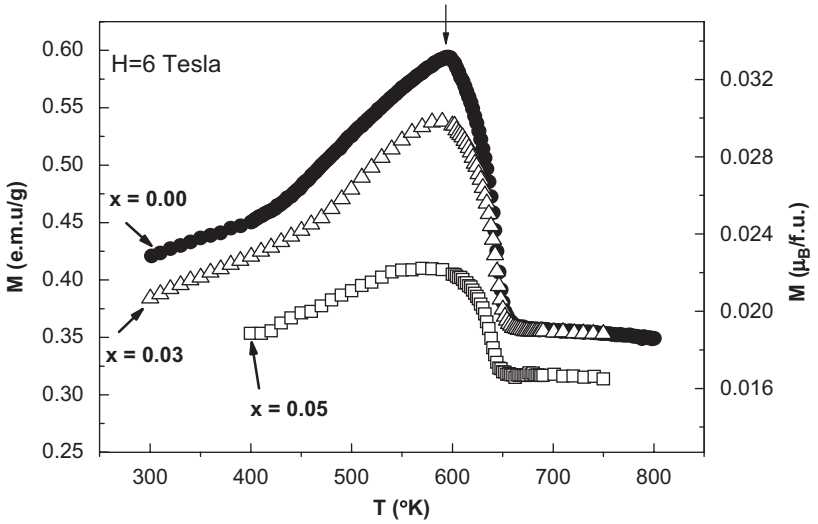


Fig. 6. $M(T)$ magnetization vs. temperature curves measured in 6 T magnetic field for samples of $Bi_{1-x}K_xFeO_3$ phase for $x = 0$, 0.03 and 0.05. The arrow in $x = 0$ curve indicates a change in the slope.

($0 \leqslant x \leqslant 0.07$) grown by the flux method. The results of the structural refinement on single crystals show that the average rhombohedral structure with $R3c$ space group evolves towards a pseudo-cubic symmetry due to a disorder related to the $K^+$ doping. Consequently, the average polar character of the ferroelectric compound $BiFeO_3$ decrease with $K^+$ rate. The average relative polar shift of cations and anions is reduced. The magnetic measurements show that related to these structural changes one can observe a decrease in the magnetization of the samples doped by potassium $K^+$, which remains antiferromagnetic with an enhancement in the antiferromagnetic behavior when the $K^+$ content increases.

## References


[1] N.A. Hill, J. Phys. Chem. B 104 (2000) 6694.
[2] V.A. Isupov, Status Solidi A 181 (2000) 211.
[3] T. Arima, A. Tokunaga, T. Goto, H. Kimura, Y. Noda, Y. Tokura, Phys. Rev. Lett. 96 (2006) 097202.
[4] T. Kimura, G. Lawes, T. Goto, Y. Tokura, A.P. Ramirez, Phys. Rev. B 71 (2005) 224425.
[5] T. Kimura, T. Goto, H. Shintani, K. Ishizaka, T. Arima, Y. Tokura, Nature (London) 55 (2003) 426.
[6] M. Mostovoy, Phys. Rev. Lett. 96 (2006) 067601.
[7] I. Sosnowska, T. Peterlin-Neumaier, E. Steichele, J. Phys. C: Solid State Phys. 15 (1982) 4835.
[8] Przenioslor, Regulskim, I. Sosnowska, J. Phys. Soc. Jpn. 75 (8) (2006) 84718.
[9] P. Fischer, M. Polemska, I. Sosnowska, M. Szymanski, J. Phys. C: Solid State Phys. 13 (1980) 1931.
[10] F. Kubel, H. Schmid, Acta Crystallogr. B 46 (1990) 698.
[11] C. Tabares-Munoz, J.P. Rivera, A. Bezinge, H. Schmid, A. Monnier, J. Appl. Phys. 24 (1985).
[12] I. Sosnowska, M. Loewenhaupt, W.I.F. David, R.M. Ibberson, Physica B 117 (1992) 180–181.
[13] I. Sosnowska, R. Przenioslo, P. Fischer, V.A. Murashov, J. Magn. Magn. Mater. 160 (1996) 384.
[14] I. Sosnowska, A.K. Zvezdin, J. Magn. Magn. Mater. 167 (1995) 140–144.
[15] C. Michel, J.M. Moreau, G.D. Achenbach, R. Gerson, W.J. James, Solid State Commun. 7 (1969) 701–704.
[16] A.V. Zalesski, A.K. Zvezdin, A.A. Frolov, A.A. Bush, JETP Lett. 71 (11) (2000) 465–468.
[17] J.M. Moreau, C. Michel, R. Gerson, W.J. James, J. Phys. Chem. Solids 32 (1971) 1315.
[18] J.B. Neaton, C. Ederer, U.V. Waghmare, N.A. Spaldin, K.M. Rabe, Phys. Rev. B 71 (2005) 014113.
[19] M. Mahesh Kumar, V.R. Palkar, K. Srinivas, S.V. Suryanarayana, Appl. Phys. Lett. 76 (2000) 2764.
[20] V.R. Palkar, D.C. Kundaliya, S.K. Malik, J. Appl. Phys. 93 (2003) 7.
[21] D. Lebeugle, D. Colson, A. Forget, M. Viret, P. Bonville, J.F. Marucco, S. Fusil, Phys. Rev. B 76 (2007) 024116.
[22] J. Wang, J.B. Neaton, H. Zheng, V. Nagarajan, S.B. Ogale, B. Liu, D. Viehland, V. Vaithyanathan, D.G. Schlom, U.V. Waghmare, N.A. Spaldin, K.M. Rabe, M. Wuttig, R. Ramesh, Science 299 (2003) 1719.
[23] T. Zhao, A. Scholl, F. Zavaliche, K. Lee, M. Barry, A. Doran, M.P. Cruz, Y.H. Chu, C. Ederer, N.A. Spaldin, R.R. Das, D.M. Kim, S.H. Baek, C.B. Eom, R. Ramesh, Nat. Mater. 5 (2006) 823.
[24] H. Béa, S. Fusil, K. Bouzehouane, M. Bibès, M. Sirena, G. Herranz, E. Jacquet, J.P. Contour, A. Barthélémy, Jpn. J. Appl. Phys. 45 (7) (2006) L187.
[25] F. Bai, J. Wang, M. Wuttig, J. Li, N. Wang, A.P. Pyatakov, A.K. Zvezdin, L.E. Cross, D. Viehland, Appl. Phys. Lett. 86 (2005) 032511.
[26] Shvartsman, V.V. Kleemann, W. Haumont, R. Kreisel, J. Appl. Phys. Lett. 90 (2007) 172115.
[27] S.K. Singh, H. Ishiwara, Jpn. J. Appl. Phys. 44 (Pt. 2) (2005) L734.
[28] S.T. Zhang, M.H. Lu, W.D. Chen, Y.F.N.B. Ming, Appl. Phys. Lett. 87 (26) (2005) 262907.
[29] Y.P. Wang, L. Zhou, M.F. Zhang, X.Y. Chen, J.M. Liu, Z.G. Liu, Appl. Phys. Lett. 84 (2004) 1731.
[30] S.K. Singh, H. Ishiwara, K. Maruyama, Appl. Phys. Lett. 88 (2006) 262908.
[31] K. Yamaguchi, K. Matsumoto, T. Fujii, IEEE Trans. Magn. 28 (5) (1992) 2447.
[32] R.D. Shannon, Acta Crystallogr. A 32 (1976) 751.
[33] C. Zener, Phys. Rev. 82 (1951) 403.
[34] P.W. Anderson, H. Hasegawa, Phys. Rev. 100 (1955) 675.
[35] P.G. de Gennes, Phys. Rev. 118 (1960) 141.
[36] J. Laugier, B. Bochu, CelRef Programs, 〈http://www.inpg.fr/LMGP〉; J. Laugier, A. Filhol, Program Celref, ILL, Grenoble, France, 1978.
[37] SOCABIM, Evaluation Programs (EVA), Society SOCABIM, 2005.
[38] T. Roisnel, J. Rodriguez-Carvajal, in: R. Delhez, E.J. Mittenmeijer (Eds.), Materials Science Forum, Proceedings of the 7th European Powder Diffraction Conference (EPDIC 7), 2000, p. 118.
[39] A.J.M. Duisenberg, L.M.J. Kroon-Batenburg, A.M.M. Schreurs, J. Appl. Cryst. 36 (2003) 220.
[40] S. Mackay, C.J. Gilmore, C. Edwards, N. Stewart, K. Shankland, Maxus Computer Program for the Solution and Refinement of Crystal Structures, Bruker Nonius, The Netherlands, 1999.
[41] P. Coppens, in: F.R. Ahmed, S.R. Hall, C.P. Huber (Eds.), Crystallographic Computing, Munksgaard, Copenhagen, 1970, pp. 255–270.
[42] R.H. Blessing, Acta Crystallogr. A 51 (1995) 33–38.
[43] G.M. Sheldrick, Programs for Crystal Structure Analysis (Release 97-2), SHELXL-93, Institüt für Anorganische Chemie der Universität, Tammanstrasse 4, D-3400 Göttingen, Germany, 1998;
G.M. Sheldrick, Acta Crystallogr. A 46 (1993) 446.
[44] J.D. Bucci, B.K. Robertson, W.J. James, J. Appl. Cryst. 5 (1972) 187.
[45] H.D. Megaw, C.N.W. Darlington, Acta Crystallogr. A 31 (1975) 161.
[46] C. Blaauw, F. Van der Woude, J. Phys. C: Solid State Phys. 6 (1973).
[47] C. Boudias, D. Monceau, Carine Crystallography, Society DIVERGENTSA, 1989–1998.